Structure and Biochemical Properties of PRL-1, a Phosphatase Implicated in Cell Growth, Differentiation, and Tumor Invasion[†,‡]

Jin-Peng Sun,[§,||] Wei-Qing Wang,[§,||] Heyi Yang,[§] Sijiu Liu,[§] Fubo Liang,[§] Alexander A. Fedorov,[⊥] Steven C. Almo,[⊥] and Zhong-Yin Zhang*[,§,⊥]

Department of Molecular Pharmacology and Department of Biochemistry, Albert Einstein College of Medicine, 1300 Morris Park Avenue, Bronx, New York 10461

Received May 17, 2005; Revised Manuscript Received July 19, 2005

ABSTRACT: The PRL (phosphatase of regenerating liver) phosphatases constitute a novel class of small, prenylated phosphatases that are implicated in promoting cell growth, differentiation, and tumor invasion, and represent attractive targets for anticancer therapy. Here we describe the crystal structures of native PRL-1 as well as the catalytically inactive mutant PRL-1/C104S in complex with sulfate. PRL-1 exists as a trimer in the crystalline state, burying 1140 Å^2 of accessible surface area at each dimer interface. Trimerization creates a large, bipartite membrane-binding surface in which the exposed C-terminal basic residues could cooperate with the adjacent prenylation group to anchor PRL-1 on the acidic inner membrane. Structural and kinetic analyses place PRL-1 in the family of dual specificity phopsphatases with closest structural similarity to the Cdc14 phosphatase and provide a molecular basis for catalytic activation of the PRL phosphatases. Finally, native PRL-1 is crystallized in an oxidized form in which a disulfide is formed between the active site Cys104 and a neighboring residue Cys49, which blocks both substrate binding and catalysis. Biochemical studies in solution and in the cell support a potential regulatory role of this intramolecular disulfide bond formation in response to reactive oxygen species such as H_2O_2.

Reversible protein tyrosine phosphorylation is a vital regulatory mechanism that lies at the center of almost all eukaryotic cellular processes (*1*). The level of tyrosine phosphorylation is modulated by the combined action of protein tyrosine kinases and protein tyrosine phosphatases (PTPs),[1] which constitute a large and structurally diverse family of signaling enzymes (*2*). Genetic and biochemical studies indicate that PTPs are essential for many physiological processes and are involved in a number of human diseases (*3*). The hallmark that defines the PTP superfamily is the active site sequence **C**(X)$_5$**R**(S/T), also known as the PTP signature motif, in the catalytic domain. Based on this unique structural feature, it is estimated that more than 100 PTPs are encoded in the human genome. The PTP superfamily can be broadly divided into two groups: the classical phosphotyrosine specific PTPs, and dual specificity phosphatases that catalyze the hydrolysis of phosphoserine/phosphothreonine as well as phosphotyrosine.

The PRL (phosphatase of regenerating liver) phosphatases represent a unique subfamily of PTPs with an apparent molecular mass of 22 kDa (*4*, *5*). This subfamily includes only three members (PRL-1, PRL-2, and PRL-3), which share a high degree (>75%) of amino acid sequence identity. The PRL phosphatases contain a consensus C-terminal prenylation motif CaaX, where C is cysteine, the a's are aliphatic residues, and X can be any amino acids. Indeed, all three enzymes are prenylated at their C terminus, which is important for their localization to the plasma membrane and early endosomal compartments (*5*-*7*). Interestingly, PRL-1 can also relocalize to the nucleus in mitotic HeLa cells in a prenylation-independent manner, raising the possibility that the cellular location of PRL-1 may be regulated in a cell cycle-dependent fashion (*8*).

PRL-1 was originally identified as an immediate early gene, which is induced during liver regeneration after partial hepatectomy (*4*). PRL-1 expression is elevated in several tumor cell lines, and overexpression of PRL-1 in NIH 3T3 fibroblasts leads to anchorage-independent growth (*4*, *8*). In addition to cell proliferation and transformation, PRL-1 may also be involved in the regulation of epithelial cell differentiation in the digestive system (*9*, *10*) and in skeletal development (*11*). The closely related PRL-2 and PRL-3 may also play a role in the regulation of cell growth and

[†] This work was supported by National Institutes of Health Grant CA69202 and the G. Harold and Leila Y. Mathers Charitable Foundation, and P50 GM62529. The structural work was based upon research conducted at beamline X9A of the National Synchrotron Light Source (Brookhaven National Laboratory) and at the Cornell High Energy Synchrotron Source (CHESS), which is supported by the National Science Foundation under award DMR-0225180 and the National Institutes of Health through its National Center for Research Resources.

[‡] The coordinates for the structures of PRL-1 (accession numbers 1X24 and 1RXD) and PRL-1/C104S in complex with sulfate (accession number 1ZCL) have been deposited in the Protein Data Bank.

* Author to whom correspondence should be addressed. Current address: Department of Biochemistry and Molecular Biology, Indiana University School of Medicine, 635 Barnhill Drive, Indianapolis, IN 46202. Office: (317) 274-8025. Fax: (317) 274-4686. E-mail: zyzhang@iupui.edu.

[§] Department of Molecular Pharmacology.

[||] These authors contributed equally to this work.

[⊥] Department of Biochemistry.

[1] Abbreviations: PTP, protein tyrosine phosphatase; VHR, VH1-related; KAP, kinase associated phosphatase; PRL, phosphatase of regenerating liver; PTEN, phosphatase and tensin homologue deleted on chromosome 10; GST, glutathione S-transferase; EDTA, ethylenediaminetetraacetic acid; HA, hemagglutinin; *p*NPP, *p*-nitrophenyl phosphate; DiFMUP, 6,8-difluoro-4-methylumbelliferyl phosphate; OMFP, 3-*O*-methylfluorescein phosphate.

10.1021/bi0509191 CCC: $30.25
Published on Web 08/19/2005

proliferation (*5*, *12*−*14*). For example, PRL-2 level is elevated in prostate cancer (*15*), while overexpression of PRL-2 causes transformation in mouse fibroblasts and hamster pancreatic epithelial cells and promotes tumor growth in nude mice (*4*, *5*). Increased level of PRL-3 in HEK293 cells also leads to higher growth rates (*12*).

Recently, the PRL phosphatases have attracted much attention because of the observation that PRL-3 transcript is highly overexpressed in liver metastases of colorectal cancer, but not in nonmetastatic primary tumors and in normal colorectal epithelium (*16*). In fact, PRL-3 mRNA level was found to be elevated in nearly all metastatic lesions derived from colorectal cancers, regardless of the sites of metastasis (*7*, *17*). In addition, PRL-3 may also promote the invasion and metastasis of human gastric carcinomas (*18*) and mouse melanoma (*19*). Finally, CHO cells stably expressing PRL-3 or PRL-1 exhibit enhanced motility and invasive activity, and induce metastatic tumor formation in mice (*13*). It has been shown that the phosphatase activity of the PRL phosphatases is required for the observed tumor metastasis activity (*13*, *20*).

Given the roles of PRL phosphatases in cellular growth, transformation, and metastatic processes, the PRL phosphatases represent attractive targets for anticancer therapeutic development. To understand the mechanism of action of the PRL phosphatases, we began a structural and biochemical investigation of PRL-1. While this work was in progress, the basic protein fold was published for PRL-3 on the basis of NMR data (*21*). Unfortunately, the active site was disordered in the NMR structure. Subsequently, a crystal structure was reported for an inactive PRL-1 mutant with a Ser substituted for the active site Cys104 (PRL-1/C104S) (*22*). Here, we describe the crystal structures of native PRL-1 and the catalytically inactive PRL-1/C104S in complex with sulfate anion. Our data revealed a large electrostatic surface in the trimeric PRL-1 structures, which is likely important for membrane binding. In addition, the active site Cys104 was found to form a disulfide bond with a nearby residue Cys49 in the native PRL-1 structures, suggesting a potential mechanism for redox regulation. Finally, we report an in-depth structure−function analysis of PRL-1, which furnishes a molecular basis for catalytic activation of the PRL phosphatases. Taken together, our studies provide novel insights into the mechanism of catalysis, regulation, and cellular localization of this important class of PRL phosphatases.

MATERIALS AND METHODS

Materials. *p*-Nitrophenyl phosphate (*p*NPP) was purchased from Fluke Co. 3-*O*-Methylfluorescein phosphate (OMFP) was obtained from Sigma. 6,8-Difluoro-4-methylumbelliferyl phosphate (DiFMUP) was purchased from Molecular Probes. 2-Chloro-4-nitrophenyl phosphate was synthesized as described (*23*). Sequencing grade trypsin were provided by Sigma (St. Louis, MO). ZipTip$_{C18}$ was obtained from Millipore (Billerica, MA). Dulbecco's modified Eagle's medium (DMEM), fetal bovine serum, penicillin, and streptomycin were from Invitrogen. A 30% solution of H_2O_2 was purchased from Fisher. All other chemicals and reagents were of the highest grade available commercially.

Expression and Purification of PRL-1 and Mutant Proteins. The expression plasmid for the His$_6$-tagged rat PRL-1 was provided by Dr. Rebecca Taub (University of Pennsylvania School of Medicine). For crystallization, the His$_6$-tagged C-terminal truncated PRL-1 and GST-PRL-1 (residues 1−160) were subcloned into pET15b and pGEX vectors, respectively. All mutants were generated using the QuickChange site-directed mutagenesis kit from Stratagene. The sequences of the wild-type and mutant PRL-1s were confirmed by DNA sequencing. For expression, wild-type and mutant PRL-1s were transformed in *Escherichia coli* BL21-(DE3) and induced by 0.1 mM isopropyl-1-thio-β-D-galactopyranoside at room temperature for 20 h. The His$_6$-tagged proteins were purified by Ni-NTA resin based upon the procedure provided by Qiagen. Proteins were judged to be at least 90% pure by SDS−PAGE. For selenomethionine-labeled PRL-1, the pGEX-PRL-1 was transformed into B834-(DE3) cells, and the protein was purified by Glutathione Sepharose 4B followed by thrombin cleavage. The protein was further purified by Mono-S ion exchange chromatography before crystallization.

Crystallization and Data Collection. The full-length His$_6$-tagged PRL-1 proved difficult to crystallize, so several constructs with N-terminal or C-terminal truncations were prepared. The construct with an N-terminal His$_6$ tag attached to PRL-1 residues 1−160 crystallized at 4 °C in 100 mM sodium acetate trihydrate pH 4.8 and 2.0 M ammonium sulfate after 2 weeks. Adding 3% ethanol into the crystallization solutions increased the size of the crystals, and this form of the crystals diffracted to 8 Å using a home light source. The diffraction quality was significantly increased when crystals were soaked in 2.4 M ammonium sulfate with 25% glycerol overnight. The final data for this form of crystals were collected up to 3.2 Å for the native protein and 2.9 Å for the PRL-1/C104S mutant at beam line X9A of the National Synchrotron Light Source (Brookhaven National Laboratory) and at MacCHESS F2 station, respectively. The crystals of both wild-type and mutant PRL-1 exhibited diffraction consistent with space group $I2_13$ with unit-cell parameters of $a = b = c = 146.8$ Å.

Crystals of selenomethionine (SeMet)-substituted His$_6$-tagged PRL-1 were quite small and not suitable for data collection. SeMet-substituted GST-PRL-1 was generated and the GST removed by thrombin after purification of the fusion protein. The SeMet PRL-1 protein was crystallized under similar conditions to the His$_6$-tagged PRL-1 albeit with a broader pH range (4.8−5.4). The SeMet PRL-1 protein crystallized in a rectangular shape, which is different from the cubic crystals obtained from the His$_6$-tagged PRL-1. Diffraction from these crystals is consistent with space group $C222_1$ with unit-cell parameters of $a = 71.3$ Å, $b = 105.6$ Å, $c = 181.4$ Å and extends to 1.9 Å at beam line 19BM of the Advanced Photon Source (APS).

Structure Solution. The structure of the SeMet substituted PRL-1 was solved using data from a SeMet multiwavelength anomalous dispersion experiment. Data collected at three wavelengths, peak (λ1), edge (λ2), and remote (λ3), were processed and scaled with the programs DENZO and SCALEPACK (*24*). The asymmetric unit contained three monomers of the PRL-1 protein. The initial MAD phases calculated to 2.8 Å using SOLVE yielded a clear electron density map in which more than 70% of the polypeptide chain could be assigned (*25*−*27*). The model was built with the program O (*28*), and the structure was further refined

by CNS (*29*). During the initial refinement, an NCS restraint for all regions except the PTP loop (104−110), WPD loop (69−73), and two additional loops (residues 20−26, 50−55) was performed. Subsequent refinement consisted of simulated annealing, energy minimization, and individual temperature factor refinement using all data between 30 and 1.9 Å. Composite simulated annealing OMIT maps were used to correct model bias. At the final stage of refinement, the NCS restraints were released and water was added. The final model has an *R*-factor of 24.5% and an R_{free} of 25.7%. The structures of the His_6-tagged PRL-1 and C104S mutant in complex with sulfate were solved by molecular replacement using the initial 2.8 Å MAD model. The final three structures include all residues from 9 to 160 except residues 71−72 of one SeMet PRL-1 molecule among three molecules in one asymmetric unit.

Kinetic Constants for PRL-1 Catalyzed Reaction. Initial rate measurements for the enzyme-catalyzed hydrolysis of *p*NPP were conducted as described previously (*30*). All assays were carried out at 25 °C in a pH 7.0 buffer of 50 mM 3,3-dimethylglutarate, containing 2 mM DTT and 1 mM EDTA, with an ionic strength of 0.15 M, adjusted by addition of NaCl. For *p*NPP reaction, assay mixtures of 200 μL in total volume were set up in a 96-well polystyrene plate from Fisher Scientific. A substrate concentration range from 0.2 to 5 K_m was used to determine the k_{cat} and K_m. Reactions were started by the addition of an appropriate amount of PRL-1. The reaction mixtures were quenched with 50 μL of 5 M sodium hydroxide, and the absorbance at 405 nm was read using a plate reader. With 4-chlorophenyl phosphate, 6,8-DiFMUP, and OMFP as substrates, PRL-1 activity was determined using a continuous assay by monitoring the absorbance at 405, 360, and 477 nm, respectively, as described (*30*). The steady-state kinetic parameters were determined from a direct fit of the data to the Michaelis−Menten equation using the nonlinear regression program KINETASYST (IntelliKinetics, State College, PA).

In Vitro Inactivation of PRL-1 by H_2O_2. To study the effect of H_2O_2 on PRL-1 activity, DTT was removed from PRL-1 preparations by Superdex-75 gel filtration. PRL-1 inactivation by H_2O_2 was studied at 25 °C in a pH 7.0 buffer of 50 mM 3,3-dimethylglutarate, 1 mM EDTA, with an ionic strength of 0.15 M, adjusted by addition of NaCl. The rate of PRL-1 inactivation by H_2O_2 was determined by following the decrease of PRL-1 phosphatase activity in the presence of 6,8-DiFMUP. The PRL-1-catalyzed hydrolysis of 6,8-DiFMUP was monitored by fluorescence at 470 nm (excitation 390 nm) from the reaction product using a Perkin-Elmer LS50B fluorometer. The apparent first-order rate constant *k* for PRL-1 inactivation was determined by fitting the data to $F = F_0 + v_0(1 - e^{-kt})/k$, where *F* is the fluorescence at time *t*, F_0 is initial fluorescence at time zero, and v_0 is the initial velocity. The second-order rate constant k_{inact} was determined by fitting the apparent first-order rate constants determined at several H_2O_2 concentrations to $k = A + k_{inact}C$, where C is the concentration of H_2O_2.

Reactivation Kinetics of H_2O_2-Inactivated PRL-1 by DTT. PRL-1 (1 mg/mL) was incubated with H_2O_2 (250 μM) for 30 min. Excess H_2O_2 was removed by addition of 1 μg of catalase to the reaction mixture (200 μL). After the enzyme was fully inactivated, 10 mM DTT was added to the reaction mixture to reactivate the enzyme. The activity of PRL-1 was monitored using DiFMUP as a substrate by a continuous assay as described above.

Mass Spectrometry. Purified wild-type and mutant PRL-1 proteins were subjected to Superdex 75 chromatography to remove DTT. The resulting protein at 1 mg/mL concentration was treated with 100 μM H_2O_2 for 30 min, and the reaction was stopped by the addition of 1 μg of catalase. The PRL-1 protein was digested with trypsin (50:1 PRL-1:trypsin ratio) overnight at 37 °C. The digested peptides were desalted using $ZipTip_{C18}$ and analyzed by a Voyager DE STR MALDI-TOF mass spectrometer (Applied Biosystems, Foster City, CA) in positive and linear mode.

Cell Culture and Transfection. HEK293 cells were grown at 37 °C under an atmosphere of 5% CO_2 in DMEM supplemented with 10% fetal bovine serum. The plasmids encoding wild-type or mutant PRL-1s tagged at their NH_2 termini with hemagglutinin (HA) were subcloned into the pCDNA-3 plasmid, and the resulting vectors were introduced into HEK293 cells by transfection with the use of Lipofectamine (Qiagen).

Identification of Reduced and Oxidized Forms of PRL-1 by Immunoblot Analysis. Before stimulation, HEK293 cells were changed into a serum-free medium. After treatment with indicated concentrations of H_2O_2 for 5 min, the cells (2×10^6 cells in 2 mL of DMEM) were scraped into 0.4 mL of ice-cold lysis buffer including 25 mM NaAc, 150 mM NaCl, pH 5.5, 10 mM iodoacetic acid, 1% Triton X-100, and 0.1% SDS, and a protease inhibitor cocktail. The cell suspensions were incubated on ice for 30 min followed by centrifugation at 10000*g* for 15 min. Equal amounts of protein from the supernatants were subjected to SDS−PAGE under nonreducing conditions, and the separated proteins were transferred electrophoretically to a nitrocellulose membrane. The membrane was then subjected to immunoblot analysis with anti-HA antibody. Immune complexes were detected with horseradish peroxidase conjugated secondary antibodies and enhanced chemiluminescence reagents (Amersham Biosciences or Pierce).

Subcellular Fractionation. HEK293 cells transiently transfected with HA-tagged PRL-1 constructs were grown in Dulbecco's modified Eagle's medium (Invitrogen) supplemented with 10% fetal bovine serum and antibiotics. Cells were washed and scraped down in 1 mL of ice-cold Hepes buffer (10 mM Hepes, pH 7.4, 1 mM EDTA, 0.5 mM PMSF, protease inhibitor cocktail, 250 mM Sucrose). Then the cells were passed through a 27-gauge needle 20 times. The resulting cell lysate was centrifuged at 1000*g* for 5 min to pellet the nuclei and intact cells, and the supernatant was again centrifuged at 100000*g* for 60 min to obtain the S100 soluble fraction and the P100 membrane fraction. Fractions were analyzed by SDS−PAGE and detected by immunoblotting with anti-HA antibody (Santa Cruz).

Chemical Cross-Linking. To assess the oligomeric state of PRL-1 and its mutants, the proteins were cross-linked with glutaraldehyde (Sigma, 25% glutaraldehyde solution, grade I). For His_6-tagged recombinant PRL-1 proteins, the reactions were performed in 100 μL solutions containing 5 μg of proteins in pH 7.5 PBS buffer. Cross-linking was initiated by adding 0.005% glutaraldehyde. For HA-PRL-1 expressed in HEK293 cells, the P100 membrane fraction in Hepes buffer (10 mM Hepes, pH 7.4, 1 mM EDTA) was incubated with 0.01% glutaraldehyde. After standing for 30 min at 25

Table 1: Crystallographic Data and Refinement Statistics[a]

			SeMet/PRL-1		
	native PRL-1	PRL-1/C104S	edge	peak	remote
data collection	NSLS-X9A	CHESS	APS-19BM	APS-19BM	APS-19BM
wavelength (Å)	0.98	0.9735	0.98000	0.97849	0.96261
space group	*I*213	*I*213		*C*2221	
unit cell (Å)					
a	146.9	146.7		71.3	
b	146.9	146.7		105.6	
c	146.9	146.7		181.4	
resolution (Å)	30−3.2	30−2.9	30−2.8	30−1.9	30−2.8
unique reflns (*N*)	8744	10372	14426	48966	14908
completeness (%)	98.7%	88.1%	92.4%	96.9%	95.0%
	(97.5%)	(99.4%)	(90.5%)	(88.6%)	(94.2%)
R_{merge}	0.102	0.054	0.088	0.089	0.083
	(0.413)	(0.469)	(0.156)	(0.355)	(0.170)
refinement					
resolution limit (Å)	30−3.2	30−2.9		30−1.9	
reflns used for refinement (*N*)	7837	9395		44046	
	(88.5%)	(79.8%)		(87.2%)	
reflns used for R_{free}[c] (*N*)	907	977		4920	
	(10.2%)	(8.3%)		(9.7%)	
R-factor[b]/R_{free}[c] (%)	24.1/28.5	26.1/29.6		24.5/25.7	
av *B*-factors	53.64	57.62		32.87	

[a] Highest shell values are in parentheses. Completeness and R_{merge} are given for all data and for all data in the highest resolution shell. [b] *R* factor $= \sum_{hkl}|F_o - F_c|/\sum_{hkl}F_o$ where F_o and F_c are the observed and calculated structure factor amplitudes for all reflections *hkl* used in refinement. [c] R_{free} is calculated for 10% of the data which were sequestered and not used in refinement.

°C, the reactions were terminated by the addition of pH 7.5 Tris-HCl (final concentration 50 mM) and by incubation on ice for 5 min. The reaction mixtures were analyzed by SDS−PAGE and detected by immunoblotting with anti-His antibody or anti-HA antibody (Santa Cruz), respectively.

RESULTS AND DISCUSSION

Crystallization and Structure Determination. The full-length PRL-1 is a protein of 173 amino acids with a C-terminal prenylation motif (CCIQ). Numerous attempts to crystallize the N-terminal His_6-tagged full-length PRL-1 were unsuccessful. Diffraction quality crystals were obtained with a C-terminal truncated PRL-1 construct (residues 1−160) containing an N-terminal His_6 tag. The C-terminal truncated PRL-1, hereby referred to as wild-type or native PRL-1, exhibited phosphatase activity similar to that of the full-length enzyme. Good quality crystals were also obtained for an inactive PRL-1 with Ser substituted for the active site Cys104 (PRL-1/C104S). The wild-type PRL-1 and PRL-1/C104S crystals formed in space group $I2_13$ and diffracted to 3.2 and 2.9 Å, respectively. Selenomethionine (SeMet)-substituted PRL-1 was expressed as a glutathione S-transferase (GST) fusion protein, purified and cleaved with thrombin to remove the GST-tag. The SeMet PRL-1 crystallized in a rectangular shape, which is different from the cubic crystals obtained from the His_6-tagged PRL-1 proteins. Diffraction from the SeMet-substituted PRL-1 crystals was consistent with space group $C222_1$ and extended to 1.9 Å resolution.

The structure of PRL-1 was solved by the multiwavelength anomalous dispersion (MAD) method using data derived from the SeMet-substituted PRL-1. Data collected at three wavelengths, peak (λ1), edge (λ2), and remote (λ3), were processed and scaled with the programs DENZO and SCALEPACK (*24*). There were three PRL-1 molecules in each asymmetric unit. The initial MAD phases were calculated to 2.8 Å using SOLVE (*25-27*). The model was built with program O (*28*) and further refined by CNS (*29*). The final structure of the native PRL-1 was refined to 1.9 Å resolution with an *R*-factor of 24.5% and an R_{free} of 25.7%. The crystal structures of the His_6-tagged PRL-1 and the C104S mutant in complex with sulfate, refined to 3.2 and 2.9 Å resolution, respectively, were solved by molecular replacement using the initial 2.8 Å MAD model. The details of the crystals and structure solution are summarized in Table 1.

Overall Structure of PRL-1. PRL-1 has a compact $\alpha + \beta$ structure comprising a central five-stranded β sheet surrounded by four α helixes on one side and two α helixes on the other (Figure 1A). Like other members of the PTP superfamily, the PTP signature motif of PRL-1 (H^{103}-$CVAGLGR^{110}$) forms a loop (P-loop) at the base of the active site pocket. The topology of PRL-1 resembles those of the catalytic domains of dual specificity phosphatases. A comparison using DALI (*31*) reveals that the PRL-1 structure is most similar to the catalytic domain of Cdc14 (*32*), KAP (*33*), and PTEN (*34*) with *Z*-scores of 17.8, 16.5, and 15.3, respectively. The structure of PRL-1 was superimposed to Cdc14 (residues 216−370, Figure 1B), KAP (residues 30−190), and PTEN (residues 25−185) with root-mean-square deviation values of 1.8, 2.1, and 1.9 Å for C_a pairs, respectively. A structure-based amino acid sequence alignment of the PRL phosphatases with Cdc14, KAP, and PTEN, as well as the prototypical dual specificity phosphatase VHR (*35*), is shown in Figure 1C. In general, there are good alignments in the core regions between the PRLs and the dual specificity phosphatases. However, substantial differences are observed in various surface loop regions. The two N-terminal loops, loop 1 ($\beta_2-\alpha_1$) and loop 2 ($\beta_3-\alpha_2$), are the most variable regions among the dual specific phosphatases. These loops define the entrance of the active site and are important for substrate binding as revealed in the structure of KAP in complex with its physiological substrate

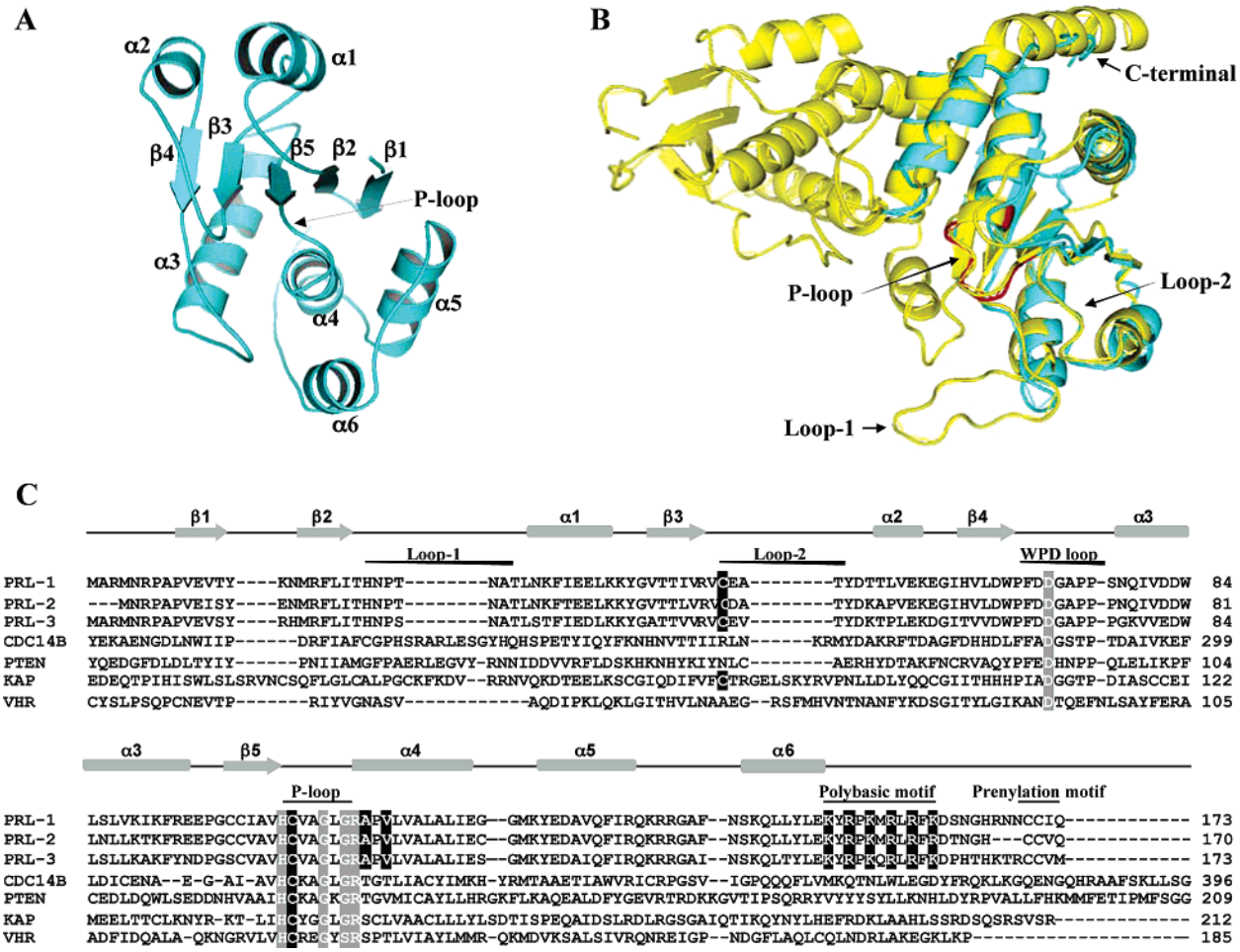

FIGURE 1: Structure of PRL-1. (A) Ribbon diagram of the PRL-1 structure. (B) Superposition of the PRL-1 (in blue) and the catalytic domain of Cdc14 (*32*) (in yellow). (C) Structure-based sequence alignment of the PRL phosphatases with other dual specificity phosphatases including Cdc14B, PTEN, KAP, and VHR.

Cdk2 (*33*). Compared with Cdc14, KAP, and PTEN, loops 1 and 2 in PRL-1 are significantly shorter (Figure 1B,C), which may contribute to PRL-1's specificity for its binding partners or substrates. These shorter loops also render PRL-1 with a more open and shallow active site.

PRL-1 Exists as a Trimer in the Crystal. The structures reported here revealed an identical trimeric arrangement of the PRL-1 molecules (Figure 2A) in two different crystallographic space groups ($I2_13$ for the His_6-tagged native PRL-1 and PRL-1/C104S, and $C222_1$ for the SeMet-substituted PRL-1) despite considerable differences in macromolecular packing. Moreover, while this manuscript was in preparation, Jeong et al. reported a structure of PRL-1/C104S (residues 4−163), which also crystallized as a trimer under totally different conditions in the $P2_1$ space group (*22*). These observations indicate that the trimeric state is structurally relevant. PRL-1 trimerization occurs around a 3-fold rotational axis that fixes the C-terminal sequence of each monomer on the same surface of the trimer (Figure 2B). Since the C-terminal sequence contains the prenylation motif (Figure 1C), it is likely that the C-terminal surface directly faces the plasma membrane. The PRL-1 active site points to the outside of the trimer interface and is positioned opposite to the C-terminal membrane association region (Figure 2B). The vertical distance between the active site and C-terminal surface is 21 Å.

The PRL-1 trimer is stabilized by a combination of hydrophobic and polar interactions. The total buried accessible surface area between the monomers at each dimer interface is 1130−1150 Å^2, which amounts to about 29% of the total surface area of each monomer. Upon trimer formation, helix α_5 of one monomer (residues 124−134) interacts with the α_1 helix, the β_1−β_2 hairpin, and the α_3−β_5 loop of another monomer (Figure 2C). Notably, Arg138 of α_5 protrudes into the hydrophobic pocket created by Lys39 and Tyr40 in the α_1 helix, forming a salt bridge with Glu36. At the other side, Pro96 from loop α_3−β_5 inserts into a hydrophobic pocket created by Leu146 in α_6, Val130 and Tyr126 in α_5. In addition to these interactions, the side chains of Asp128, Gln131, Arg134, and Gln135 make 5 hydrogen bonds with the main chain amides or carbonyls of the β_1−β_2 hairpin and the α_3−β_5 loop, and one hydrogen bond with the side chain of Arg18. It is important to point out that the observed dimer interface interactions involve residues (e.g. Arg18, Glu36, Pro96, Met124, Tyr126, Asp128, Val130, Arg138, and Leu146) that are conserved among all PRL family members and across all species. Consequently, trimer formation may be a general property of all PRL enzymes.

The observation that PRL-1 exists in a trimeric state in the crystal is novel among the PTPs. However, it is not clear whether PRL-1 is also capable of trimer formation in solution and/or in the cell. To address this question, we performed

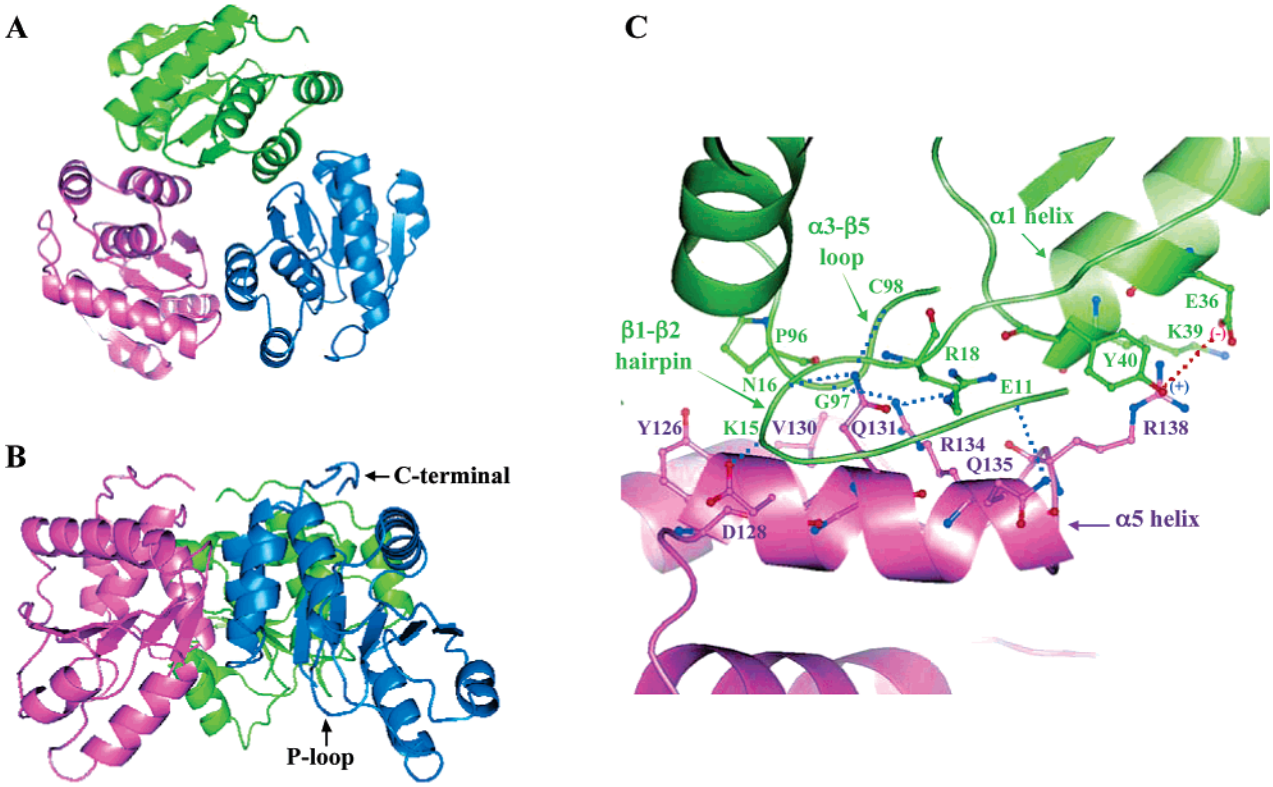

FIGURE 2: Global view of the PRL-1 trimer. (A) The front view, in which the noncrystallographic 3-fold axis is perpendicular to the plane of the figure. (B) The side view, in which the C-terminal tails point to the same direction that is opposite to where the active sites are located. (C) Close-up view of the interactions at the dimer interface between each pair of the PRL-1 monomers.

gel filtration, ultracentrifugation, and dynamic light scattering experiments at PRL-1 concentrations of 0.1−3 mg/mL. Under these conditions PRL-1 appeared mostly as monomers (data not shown). Similarly, PRL-3 was observed as a monomer in NMR experiments even at mM concentrations (*21*, *36*). To further evaluate the potential for PRL-1 trimerization, we conducted cross-linking experiments with both purified recombinant PRL-1 protein and membrane fractions derived from HEK293 cells expressing the full-length HA-tagged PRL-1. The cross-linked proteins were resolved by SDS−PAGE. As shown in Figure 3A,B, cross-linking of purified PRL-1 protein as well as full-length PRL-1 in cell membranes with glutaraldehyde resulted in new bands with molecular weights corresponding to PRL-1 dimer, trimer, and higher oligomers. This indicates that although in solution the equilibrium may favor the monomer, PRL-1 has the intrinsic ability to form dimer, trimer, or higher oligomers.

We next determined if structural perturbations to the dimer interface would affect trimer formation. We introduced mutations into PRL-1 that were expected to either ablate the salt bridge between Glu36 and Arg138 (E36A/R138A) or disrupt the polar interactions between Arg18 and Gln131 (R18A/Q131A) (Figure 2C). To introduce more dramatic changes into the dimer interface, we also replaced Gly97 with an Arg. We expressed and purified each of the mutant proteins and determined that these mutations had little effect on the catalytic activity of PRL-1 (Table 2). As shown in Figure 3A, R18A/Q131A and E36A/R138A exhibited similar oligomerization potential as the wild-type PRL-1, indicating that interruption of neither the salt bridge between Glu36 and Arg138 nor the polar interactions between Gln131 and Arg18 was sufficient to abolish PRL-1 trimer formation. In

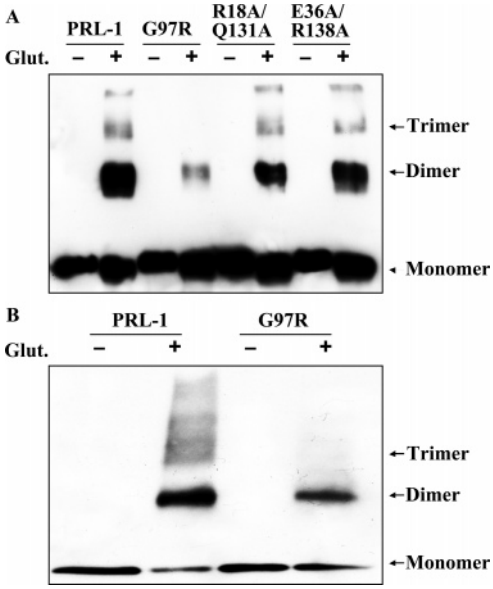

FIGURE 3: Trimer formation of PRL-1 in solution and inside the cell. (A) Cross-linking of purified full length PRL-1 protein. PRL-1 (2 μM) was cross-linked with 0.005% glutaraldehyde for 30 min at 25 °C. The cross-linked species was visualized by staining with Coomassie brilliant blue. (B) Cross-linking of PRL-1 in membrane fractions of HEK293 cells expressing HA-tagged full-length PRL-1. Three microliters of membrane fractions (1 mg/mL) were cross-linked with 0.01% glutaraldehyde for 30 min at 25 °C. The PRL-1 proteins were detected by Western blotting using anti-HA antibodies.

contrast, introduction of a more bulky Arg residue to position 97 substantially reduced PRL-1 trimerization both in solution and in cell membrane fractions (Figure 3A,B). Collectively, the results show that even though PRL-1 may exist primarily

Table 2: Steady-State Parameters for the PRL-1-Catalyzed Hydrolysis of *p*NPP at pH 7.0 and 25 °C

PRL-1	k_{cat} (s^{-1})	K_m (mM)	k_{cat}/K_m (M^{-1} s^{-1})
WT	$(0.71 \pm 0.02) \times 10^{-4}$	0.54 ± 0.07	0.133
PRL-1/1−160	$(0.74 \pm 0.04) \times 10^{-4}$	0.57 ± 0.02	0.130
PRL-1/1−169	$(0.59 \pm 0.02) \times 10^{-4}$	0.56 ± 0.02	0.105
PRL-1/6A	$(0.56 \pm 0.01) \times 10^{-4}$	0.52 ± 0.05	0.107
PRL-1/A111S	$(1.09 \pm 0.05) \times 10^{-3}$	3.53 ± 0.15	0.309
PRL-1/V113T	$(3.15 \pm 0.35) \times 10^{-4}$	0.34 ± 0.03	0.926
PRL-1/R137A	$(0.74 \pm 0.01) \times 10^{-5}$	2.50 ± 0.50	0.00296
PRL-1/C49S	$(0.35 \pm 0.01) \times 10^{-4}$	0.98 ± 0.10	0.036
PRL-1/G97R	$(0.55 \pm 0.01) \times 10^{-4}$	0.58 ± 0.02	0.094
R18A/Q131A	$(0.45 \pm 0.01) \times 10^{-4}$	0.46 ± 0.01	0.098
E36A/R138A	$(0.98 \pm 0.02) \times 10^{-4}$	0.52 ± 0.03	0.188

as monomers under our experimental solution conditions, it clearly has intrinsic propensity to form trimers.

In the cell, the PRL phosphatases are prenylated at their C termini (*5*−*7*), which should anchor them to the plasma membrane. The increase in local PRL-1 concentration in the membrane upon PRL-1 prenylation would be expected to significantly promote trimerization. We speculate that the PRL-1 trimers observed in the crystal forms would most likely mimic the trimerization of intact PRL-1 localized in the membrane given that the C-terminal prenylation motif resides on the lipid-facing surface. It is possible that PRL-1 trimerization in the cell may represent a novel mechanism for regulation, although its biological significance will require further investigation.

The Polybasic Region in the C-Terminal of PRL-1 Is Required for Plasma Membrane Association. The PRL phosphatases have a conserved C-terminal polybasic region composed of multiple lysines and arginines (Lys151, Arg153, Lys155, Arg157, Arg159 and Lys161), which immediately precedes the CaaX sequence (Figure 1C). These basic residues are solvent exposed, and together with Lys90, Arg93, and Lys125 they are clustered on the C-terminal side of the trimer forming a strikingly basic patch that should interact favorably with the acidic membrane surface (Figure 4A). This structural feature was not apparent in the previously reported PRL-1/C104S structure, which contains residues 8−156 (*22*). To investigate whether this polybasic region is required for membrane association, we transfected the HA-tagged full-length wild-type as well as mutant PRL-1 constructs into HEK293 cells and determined their subcellular localization. To ensure that mutations would not cause gross structural perturbations, all mutant recombinant PRL-1 proteins were purified, characterized, and found to have phosphatase activity similar to that of the wild-type enzyme (Table 2).

Consistent with previous findings (*5*, *6*), full-length PRL-1, which should be prenylated inside the cells, was found predominantly in the membrane fraction, whereas a mutant lacking the C-terminal prenylation motif (PRL-1/1−169) localized entirely to the soluble cytoplasmic fraction (Figure 4B). This confirms the importance of the C-terminal prenylation for PRL-1 plasma membrane localization. To determine whether PRL-1 trimerization affects its membrane localization, we also examined the subcellular fractionation of PRL-1/G97R, which is defective in trimer formation. As shown in Figure 4B, disruption of trimer formation had no effect on PRL-1 association with the membrane. In stark contrast, when all six positively charged residues in the polybasic stretch were replaced with alanines, the resulting mutant PRL-1/6A was found completely in the soluble fraction (Figure 4B). The observation that PRL-1/6A failed to localize to the membrane suggests that PRL-1 prenylation alone is insufficient for plasma membrane localization and that the C-terminal polybasic region is required for proper membrane targeting of PRL-1. Collectively, our results indicate that localization of PRL-1 to the plasma membrane requires both insertion of the prenylation group into the lipid bilayer and ionic interactions between the polybasic region and the acidic membrane surface. Interestingly, the dual requirement of hydrophobic and electrostatic interactions for correct membrane targeting has also been noted for a number of important signaling proteins including small G protein K-ras and the Src kinase (*37*−*39*).

The PRL-1 Active Site. The activity of PRL-1 toward the chromogenic substrate *p*-nitrophenyl phosphate (*p*NPP) was orders of magnitude lower than those of tyrosine specific phosphatases (e.g. PTP1B (*40*) and the *Yersinia* PTP (*41*)) and dual specificity phosphatases (e.g. VHR (*42*) and Cdc14 (*30*)) (Table 2). Similar low activity toward synthetic substrates was also noted for PRL-3 (*21*). To begin to probe the active site properties of PRL-1, we determined the kinetic parameters for the PRL-1 catalyzed hydrolysis of a panel of aromatic phosphates, including 1-ringed, 2-ringed, and multiringed substrates. As shown in Table 3, the k_{cat} values are similar for all aryl phosphate substrates even though their leaving group pK_a values are markedly different. This suggests that the rate-determining step for the PRL-1 reaction is most likely hydrolysis of the phosphoenzyme intermediate (*43*), although we cannot exclude the possibility that intermediate formation is rate-limiting when the general acid is in full operation. The k_{cat}/K_m value, which is a measure of substrate specificity, differs in a dramatic manner. An examination of k_{cat}/K_m values reveals that the active site specificity of PRL-1 is distinct from those of other dual specificity phosphatases, such as Cdc25 phosphatases, MAP kinase phosphatases, and VHR, which display a striking preference (∼2−3 orders of magnitude) for the bulky 3-ringed substrate 3-*O*-methylfluorescein phosphate (OMFP) (*44*−*49*). Thus, in line with the structural similarity to Cdc14, the active site specificity of PRL-1 is also similar to that of Cdc14 (*30*), with a strong preference for two-ringed aryl phosphates (6,8-difluoro-4-methylumbelliferyl phosphate, DiFMUP) over smaller one-ringed (*p*NPP and 2-chloro-4-nitrophenyl phosphate) or larger, 3-ringed substrate (OMFP), a finding that may have important implications for inhibitor design.

To determine the molecular basis for the extremely low activity toward small molecule substrates, we analyzed the structure of PRL-1/C104S in complex with a sulfate ion bound at the active site (Figure 5A). Like the substrate phosphate group, the sulfate ion sits in the middle of the P-loop, which is composed of the PTP signature motif **C**$(X)_5$**R**. In the PTP mechanism, the Cys residue in the P-loop is situated at the base of the active site pocket and functions as a nucleophile while the Arg coordinates the substrate phosphoryl group (*43*). In addition to strong polar interactions with the P-loop amides, the sulfate ion also makes two hydrogen bonds with the guanidinium group of Arg110 in the P-loop, which in turn is engaged in hydro-

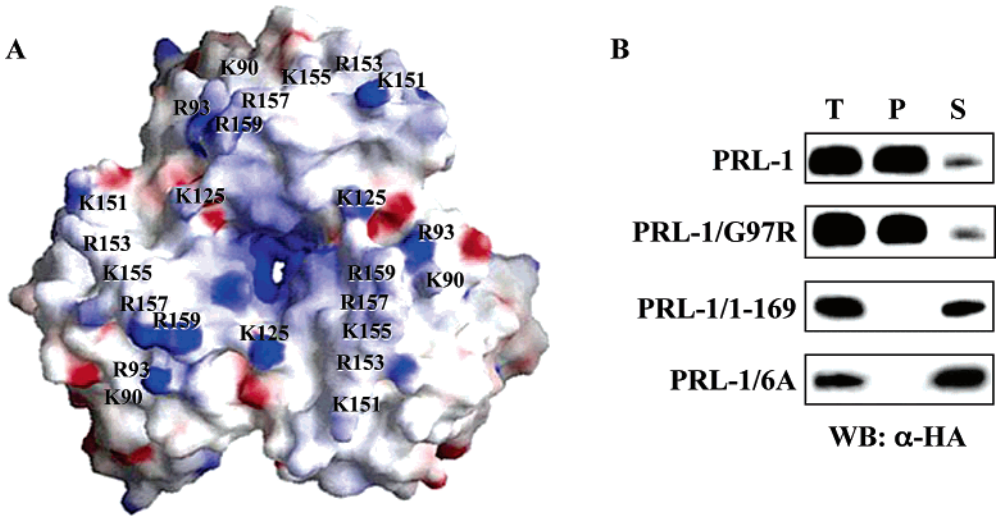

FIGURE 4: The polybasic region in the C-terminal of PRL-1. (A) GRASP (*63*) surface representation of the PRL-1 trimer with the C-terminal surface facing the reader. The surface is colored according to the electrostatic potential: blue for positive and red for negative. (B) Subcellular fractionation of HA-tagged PRL-1. The total (T), P100 membrane (P), and S100 cytosol (S) fractions were analyzed by SDS−PAGE and detected by anti-HA antibodies.

Table 3: Kinetic Parameters of the PRL-1-Catalyzed Hydrolysis of Small Molecule Aryl Phosphate Substrates[a]

Substrate	pK_a	k_{cat} (s^{-1})	K_m (mM)	k_{cat}/K_m ($M^{-1}\,s^{-1}$)
OMFP	4.6	$(1.91 \pm 0.02) \times 10^{-4}$	0.022 ± 0.07	8.76
DiFMUP	4.7	$(1.43 \pm 0.02) \times 10^{-4}$	0.0046 ± 0.0001	31.0
2-Cl-4-NO_2	5.45	$(1.15 \pm 0.03) \times 10^{-4}$	0.056 ± 0.004	2.04
*p*NPP	7.14	$(0.71 \pm 0.02) \times 10^{-4}$	0.54 ± 0.07	0.133

[a] The assays were performed at pH 7.0, 25 °C as described in Materials and Methods. Listed are the leaving group pK_a values for the substrates. The substrates include (1) 3-ringed aryl phosphate OMFP; (2) 2-ringed aryl phosphate DiFMUP; and (3) 1-ringed aryl phosphates 2-Cl-4-NO_2 (2-chloro-4-nitrophenyl phosphate) and *p*NPP.

phobic interactions with the phenyl ring of Phe70 and a polar interaction with the main chain carbonyl oxygen of Phe70 (Figure 5B). As a result of these interactions, the WPD loop is in a closed conformation, placing the carboxylate of Asp72 close (3.66 Å) to the sulfate oxygen, which is structurally homologous to the scissile oxygen of a substrate. This observation suggests that the Asp72 most likely acts as a general acid in PRL-1 catalysis.

Although many of the interactions with the oxyanion involving the P-loop and the WPD loop in PRL-1 are similar to those found in other PTPs, there are also significant differences between the active sites of PRL-1 and other members of the PTP superfamily (e.g., *Yersinia* PTP and Cdc14), which display a higher intrinsic activity toward *p*NPP. These differences may account for PRL-1's low basal activity toward artificial substrates. For example, in most PTPs a conserved Ser or Thr is placed immediately after the invariant Arg residue in the PTP signature motif. In PRLs, this position is occupied by Ala111. In the Cdc14 structure (Figure 5B) (*32*), the hydroxyl group of the conserved Thr321 is approximately 2.8 Å to the Sγ of the active site Cys314, making a good S−HO hydrogen bond. Mutagenesis and kinetic studies have shown that the conserved hydroxyl group in the P-loop plays an important role in the hydrolysis of the phosphoenzyme intermediate (*43*). In agreement with this finding, when Ala111 was replaced with a Ser, the k_{cat} of PRL-1/A111S toward *p*NPP increased 15-fold, while the k_{cat}/K_m value, which monitors the kinetic steps leading to and including the formation of the phosphoenzyme intermediate, was only 2-fold higher than that of the wild-type enzyme (Table 2).

In addition to the lack of a conserved hydroxyl group in the PTP signature motif, PRL-1 is also missing a key H-bonding network that stabilizes the P-loop. In Cdc14, the conserved Arg348 (equivalent to Arg440 in the *Yersinia* PTP and Arg257 in PTP1B) makes two well-defined H-bonds with the main chain carbonyl oxygens in the middle of the P-loop. Arg347 is in turn anchored by polar interactions with the side chains of Asn217 and Asp215 (Figure 5B). Substitution of this Arg with an Ala in the *Yersinia* PTP, PTP1B, and Cdc14 results in greater than 3 orders of magnitude decrease in k_{cat} (*50*, *51*; Wang, W.-Q., unpublished observations). In MKP3, this important Arg is replaced with a Lys, which was proposed partially responsible for MKP3's low basal activity toward *p*NPP (*52*). While the corresponding Arg137 is present in PRL-1, its interactions with the P-loop are rather weak (Figure 5B). Furthermore, PRL-1 does not have the tertiary residues (Asn217 and Asp215 in Cdc14) that serve to stabilize the conformation of Arg137. Consequently, the contribution of Arg137 to PRL-1 catalysis is not expected to be as important as those from the corresponding Arg in the *Yersinia* PTP, PTP1B, and Cdc14. Indeed, when the side chain of Arg137 is removed, the k_{cat} for PRL-1/R137A is only 10-fold lower than that of the wild-type enzyme (Table 2).

Finally, PRL-1 also lacks a H-bond that is potentially important for the stabilization of the C-terminal part of the P-loop. In Cdc14 (as well as other PTPs), the C-terminal portion of the P-loop is anchored by two H-bonds between the amides of Leu352 and Thr323 and the carbonyls of Leu318 and Gly319 in the P-loop, plus an additional H-bond between the side chain of Thr323 and the carbonyl of Gly319 (Figure 5B). The latter H-bond is absent in PRL-1 because the corresponding Thr323 is substituted by a Val in PRL-1 (Val113) (Figure 5B). In support of the importance of this H-bond, introduction of a Thr residue at position 113 increased the k_{cat} and k_{cat}/K_m for the PRL-1/V113T-catalyzed *p*NPP reaction by 4.4- and 7.0-fold, respectively (Table 2).

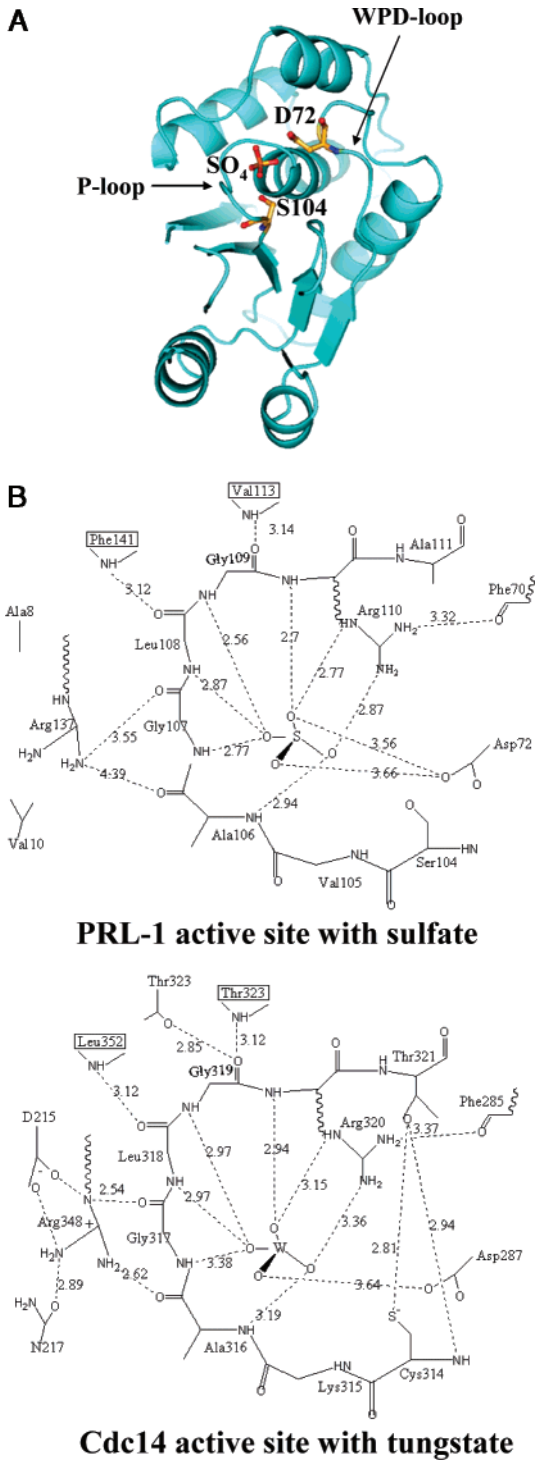

FIGURE 5: The structure of the PRL-1 active site. (A) Ribbon representation of the PRL-1/C104S structure in complex with sulfate, in which the active site Cys104 on the P-loop, the general acid Asp72 on the WPD loop, and the sulfate anion are labeled. (B) Comparison of active site interactions between PRL-1 and Cdc14.

Collectively, the structural and biochemical data suggest that the active site of PRL-1 is not optimally primed for hydrolysis of nonspecific substrates. Although the physiological substrates of the PRL phosphatases remain to be identified, one would predict that the association of PRL-1 with its physiological substrates and/or activators would elicit catalytic activation of PRL-1 by facilitating the repositioning of the P-loop and other active site residues for optimal substrate turnover. Binding of a small molecule substrate or a nonspecific substrate may not be sufficient to induce a conformational change in PRL-1 so that the P-loop is properly positioned for catalysis.

Redox Regulation of PRL-1 Activity. The PRL-1 proteins were crystallized in the presence of 1 mM DTT. Unexpectedly, the crystal structures for the native PRL-1 reported here showed well-ordered electron density in the active site consistent with a disulfide bond linking the catalytic Cys104 with a neighboring Cys49 (Figure 6A). Like the active site Cys104, Cys49 is invariant among all PRLs. The presence of a disulfide bridge between Cys104 and Cys49 suggests that the active site Cys104 is highly susceptible to oxidation. Although oxidation of the PTP active site Cys generally leads to the formation of a sulfenic acid intermediate (*53*−*55*), intramolecular disulfide formation between the active site nucleophilic Cys and a nearby Cys residue has also been observed in KAP (*33*), PTEN (*56*), Cdc25 (*57*, *58*), and the low molecular weight PTPs (*59*). The distance between the C_α atoms of the two cysteine residues is 4.68 Å in PRL-1, which is in the range (4.4−5.9 Å long) of the normal C_α−C_α distance of disulfide bonds (*60*). This indicates that the redox-mediated disulfide formation between Cys104 and Cys49 in PRL-1 should be a facile process and can occur without any major conformational change. Given the importance of the catalytic Cys in PTP catalysis, blocking of the nucleophilic thiolate in Cys104 with a disulfide is expected to render PRL-1 inactive.

In addition to demolition of the nucleophilic capability of the active site Cys104, disulfide formation in PRL-1 is accompanied by localized conformational changes (P-loop and WPD-loop) in the active site (Figure 6B). As a result of the disulfide bond between Cys104 and Cys49, the C_α of Cys49 is shifted 1.25 Å toward the active site, while no other significant structure movements are observed in β_3 where Cys49 resides. Moreover, disulfide bond formation also imposes conformational constraints on the P-loop and increases the ψ angle of Cys104 from 20° to 56°. Consequently, the P-loop adopts a hairpin conformation in the native PRL-1 structures as opposed to the helical conformation in the PRL-1/C104S structure in complex with a sulfate anion (Figure 6B). In the latter structure, the sulfate is at the center of the P-loop and within 3 Å from every amide nitrogen of the P-loop. This orientation of the P-loop amides is essential for oxyanion binding. However, in the oxidized PRL-1 structures, the carbonyls of Gly107 and Leu108, instead of the amides, are pointing toward the inside of the P-loop, which reduces the positively charge character of the P-loop. As a result, although PRL-1 was crystallized in 2 M sulfate, bound sulfate was not observed in the oxidized PRL-1 crystal. Thus, disulfide formation in the PRL-1 active site also disrupts its ability to bind substrates.

The direct observation of a disulfide bond between Cys104 and Cys49 in the PRL-1 crystal structure suggests a redox mechanism for PRL-1 regulation. To test this hypothesis, we determined the effect of H_2O_2 on PRL-1 activity. H_2O_2 is implicated as an intracellular messenger that is generated in response to growth factor stimulation (*61*), and H_2O_2 can modulate intracellular protein tyrosine phosphorylation by reversible inactivation of PTPs (*62*). As expected, we found that H_2O_2 can inactivate PRL-1 in a time- and concentration-dependent first-order process (data not shown). Analysis of

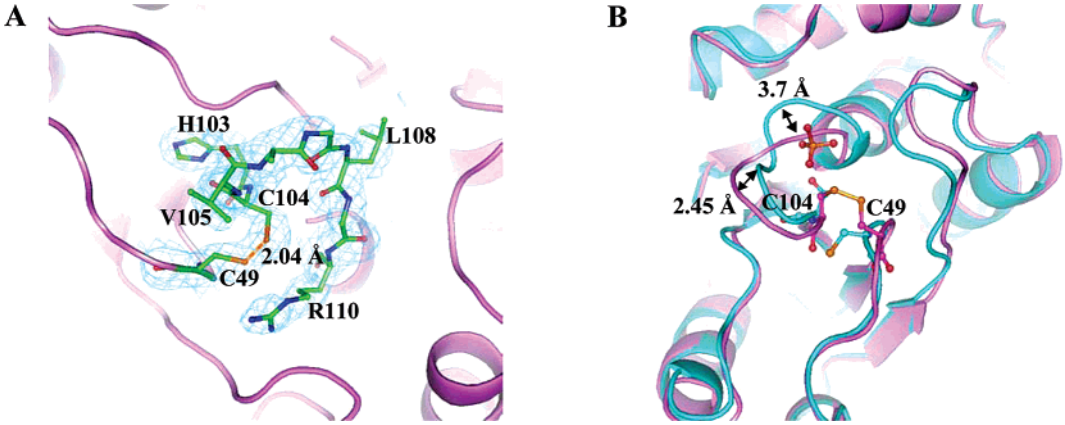

FIGURE 6: Disulfide bond formation between the active site Cys104 and a neighboring Cys49 in PRL-1. (A) Simulated annealing omit map showing unbiased density for the P-loop and the disulfide between Cys104 and Cys49. The density shown is a $F_o - F_c$ map contoured at 3.2σ. (B) Conformational changes in the PRL-1 active site as a result of the disulfide formation. The conformational changes are revealed by structural alignment of the native (oxidized) PRL-1 structure (in violet) and the structure of PRL-1/C104S bound with sulfate (in blue). Residues Cys104 and Cys49, as well as the sulfate anion, are labeled in the figure.

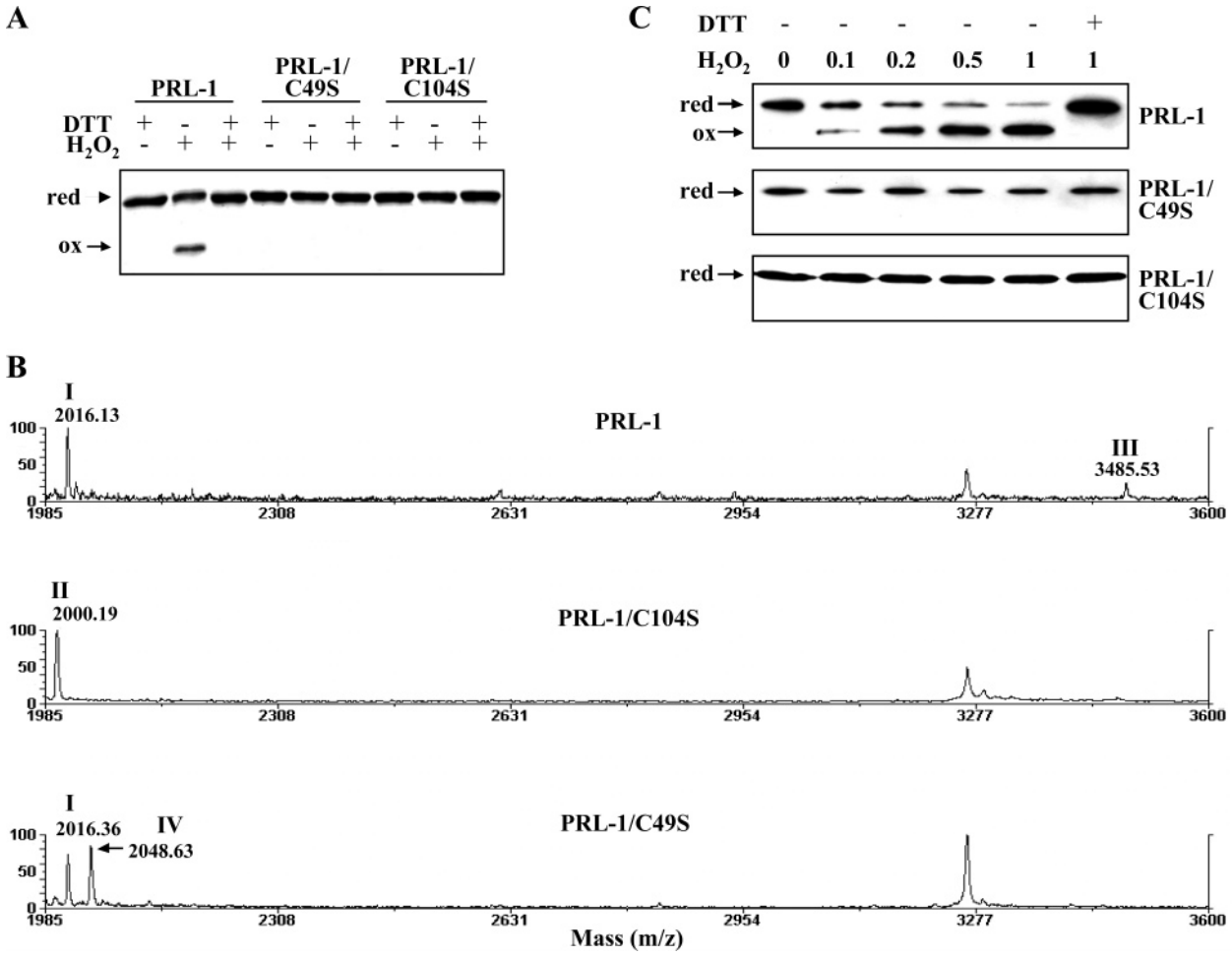

FIGURE 7: The H_2O_2-mediated disulfide formation between Cys104 and Cys49 in PRL-1. (A) Effect of mutation of Cys104 and Cys49 on the H_2O_2-induced gel mobility shift of PRL-1 under reducing conditions. (B) MALDI-TOF mass spectrometric detection of a fragment of the oxidized PRL-1 (peak III) containing a disulfide linkage between Cys104 and Cys49. (C) Disulfide bond formation between Cys104 and Cys49 of PRL-1 in HEK293 cells exposed to H_2O_2. Transfected cells expressing HA-tagged PRL or mutants were incubated with H_2O_2, after which cellular protein extracts were subjected to nonreducing SDS−PAGE and analyzed with anti-HA antibodies.

the pseudo-first-order rate constant as a function of H_2O_2 concentration yielded a second-order rate constant of 15.4 M^{-1} s^{-1}, a value similar to those measured for other PTPs (*53*). PRL-1/C49S displayed a slightly lower activity than that of the wild-type PRL-1 (Table 2). Like the native enzyme, PRL-1/C49S could also be inactivated upon H_2O_2 treatment. Similar to other PTPs, the activity of the H_2O_2-inactivated PRL-1 can be fully recovered with DTT.

To determine whether the H_2O_2-mediated PRL-1 inactivation resulted in the formation of a disulfide bond between Cys104 and Cys49, we analyzed the PRL-1 protein treated with or without H_2O_2 by SDS−PAGE under nonreducing

conditions. Since disulfide formation generally results in a more compact protein structure, we would predict that the disulfide form of PRL-1 should migrate faster on SDS−PAGE under nonreducing conditions. Indeed, H_2O_2 treatment of PRL-1 led to the appearance of a faster migrating band on nonreducing SDS−PAGE (Figure 7A). Upon reduction with DTT, the gel mobility of the H_2O_2-treated PRL-1 was restored to the same level exhibited by the native PRL-1 protein. However, when either Cys49 or Cys104 was changed to a Ser, the mobility of the PRL-1/C49S and PRL-1/C104S mutants was not affected by H_2O_2. These results thus are consistent with Cys104 in the active site of PRL-1 forming a disulfide bond with Cys49 upon oxidation with H_2O_2.

To provide more direct evidence for the formation of a disulfide bond between Cys104 and Cys49, we subjected the H_2O_2-treated PRL-1 to trypsin digestion followed by MALDI-TOF mass spectrometric analysis. As shown in Figure 7B, peak I was found to contain a peptide of molecular mass MH^+ of 2016.13 Da, which corresponds to the active site tryptic peptide F^{92}REEPGCCIAVHCVAGLGR^{110} (calculated MH^+ 2016.95 Da). Peak II corresponds to the same peptide from PRL-1/C104S in which Cys104 is replaced with a Ser (MH^+ 2000.97 Da calculated, MH^+ 2000.19 observed). Peak III with an observed MH^+ of 3485.53 is in close agreement with the MH^+ of 3485.65 calculated for a 32-residue fragment of PRL-1 in which a Cys104-containing peptide (F^{92}REEPGCCIAVHCVAGLGR^{110}, calculated MH^+ 2016.95) and a Cys49-containig peptide (V^{48}CEATYDTTLVEK^{60}, calculated MH^+ 1471.70) are bridged by a disulfide bond. In contrast, H_2O_2 treatment of PRL-1/C104S and PRL-1/C49S did not yield the disulfide-bridged peak III (Figure 7B). These results provide further support that Cys104 and Cys49 of PRL-1 form a disulfide bond upon exposure to H_2O_2. Interestingly, a new peak (peak IV, MH^+ 2048.63 Da) emerged from the trypsin digest of the H_2O_2-treated PRL-1/C49S sample, whose MH^+ is 32 mass units higher than that of the active site peptide F^{92}REEPGCCIAVHCVAGLGR^{110} (peak I). One possibility may be that one of the Cys residues in the F^{92}REEPGCCIAVHCVAGLGR^{110} sequence of PRL-1/C49S was oxidized by H_2O_2 to produce an irreversible sulfinic acid derivative. Since peak IV was absent in the PRL-1/C104S sample, the sulfinic acid in peak IV is most likely derived from the oxidation of Cys104 in PRL-1/C49S. The data thus indicate that, in the absence of Cys49, the active site Cys104 is more vulnerable to oxidation by H_2O_2. We could speculate that one intriguing function of Cys49 to form an intramolecular S−S bond with Cys104 would be to protect the catalytic Cys104 from further and irreversible oxidation.

Finally, we examined whether PRL-1 can be oxidized in cells exposed to H_2O_2. HEK293 cells transiently transfected with the HA-tagged PRL-1 were incubated for 5 min with various H_2O_2 concentrations. Subsequently, cell lysates were fractionated using SDS−PAGE under nonreducing conditions, and the separated proteins were then subjected to immunoblot analysis with anti-HA antibodies. As shown in Figure 7C, exposure of cells to H_2O_2 at concentrations as low as 100 μM led to the appearance of the higher mobility (the disulfide modified) form of PRL-1, and the intensity of the higher mobility band increased as the H_2O_2 concentration was raised. When the H_2O_2-treated cell lysates were incubated with 10 mM DTT before SDS−PAGE analysis, only the lower mobility (reduced) form of PRL-1 was detected, in accord with the notion that the higher mobility form of PRL-1 contains a disulfide bond. Consistent with our finding that the disulfide between Cys104 and Cys49 is responsible for the mobility shift of PRL-1, mutation of either Cys104 or Cys49 prevented the formation of the higher mobility band upon exposure of the cells to H_2O_2 (Figure 7C). Together, the data show that oxidation of PRL-1 in cells exposed to H_2O_2 also results in the formation of a disulfide bond between Cys104 and Cys49.

In conclusion, we have determined the crystal structures of native PRL-1 at 1.9 and 3.2 Å resolution, respectively. We have also reported the crystal structure of PRL-1/C104S in complex with sulfate solved to 2.9 Å. Structural and kinetic analyses place PRL-1 in the family of dual specificity phopsphatases with closest structural similarity to the Cdc14 phosphatase, and provide a molecular basis for the extremely low activity of the PRL phosphatases toward nonspecific substrates. It is likely that significant structural rearrangements will occur upon association of the PRL phosphatases with their physiological substrates and/or activators in order to enable efficient substrate turnover. PRL-1 is found to exist as a trimer in the crystal structures, burying 1140 A^2 of accessible surface area at each dimer interface. Mutation of Gly97 in the dimer interface to an Arg significantly reduces the oligomerization potential of PRL-1. Trimerization creates a large, bipartite membrane-binding surface in which the exposed C-terminal basic residues could cooperate with the adjacent prenylation group to anchor PRL-1 on the acidic inner membrane. Indeed, replacement of Lys151, Arg153, Lys155, Arg157, Arg159, and Lys161 by Ala residues completely abolished the ability of PRL-1 to bind plasma membrane. Our results indicate that localization of PRL-1 to the plasma membrane requires both insertion of the prenylation group into the lipid bilayer and ionic interactions between the C-terminal basic residues and the acidic membrane surface. Finally, the active site Cys104 is found in a disulfide linkage with a neighboring Cys49 in the native PRL-1 structures. Formation of this disulfide bond would be expected to block both substrate binding and catalysis. Biochemical studies indicate that H_2O_2 can promote intramolecular disulfide bond formation between Cys104 and Cys49 in solution and in the cell, which supports a potential regulatory role of Cys49 in modulating PRL-1 activity in response to reactive oxygen species.

REFERENCES

1. Hunter, T. (1998) The phosphorylation of proteins on tyrosine: its role in cell growth and disease, *Philos. Trans. R. Soc. London, Ser. B 353*, 583−605.
2. Alonso, A., Sasin, J., Bottini, N., Friedberg, I., Friedberg, I., Osterman, A., Godzik, A., Hunter, T., Dixon, J., and Mustelin, T. (2004) Protein tyrosine phosphatases in the human genome, *Cell 117*, 699−711.
3. Zhang, Z.-Y. (2001) Protein tyrosine phosphatases: prospects for therapeutics, *Curr. Opin. Chem. Biol. 5*, 416−423.
4. Diamond, R. H., Cressman, D. E., Laz, T. M., Abrams, C. S., and Taub, R. (1994) PRL-1, a unique nuclear protein tyrosine phosphatase, affects cell growth, *Mol. Cell. Biol. 14*, 3752−3762.
5. Cates, C. A., Michael, R. L., Stayrook, K. R., Harvey, K. A., Burke, Y. D., Randall, S. K., Crowell, P. L., and Crowell, D. N. (1996) Prenylation of oncogenic human PTP(CAAX) protein tyrosine phosphatase, *Cancer Lett. 110*, 49−55.
6. Zeng, Q., Si, X., Horstmann, H., Xu, Y., Hong, W., and Pallen, C. J. (2000) Prenylation-dependent association of protein-tyrosine

phosphatases PRL-1, -2, and -3 with the plasma membrane and the early endosome, *J. Biol. Chem. 275*, 21444−21452.
7. Bardelli, A., Saha, S., Sager, J. A., Romans, K. E., Xin, B., Markowitz, S. D., Lengauer, C., Velculescu, V. E., Kinzler, K. W., and Vogelstein, B. (2003) PRL-3 expression in metastatic cancers, *Clin. Cancer Res. 9*, 5607−5615.
8. Wang, J., Kirby, C. E., and Herbst, R. (2002) The tyrosine phosphatase PRL-1 localizes to the endoplasmic reticulum and the mitotic spindle and is required for normal mitosis, *J. Biol. Chem*. *277*, 46659−46668.
9. Diamond, R. H., Peters, C., Jung, S. P., Greenbaum, L. E., Haber, B. A., Silberg, D. G., Traber, P. G., and Taub, R. (1996) Expression of PRL-1 nuclear PTPase is associated with proliferation in liver but with differentiation in intestine, *Am. J. Physiol. 271*, G121−129.
10. Kong, W., Swain, G. P., Li, S., and Diamond, R. H. (2000) PRL-1 PTPase expression is developmentally regulated with tissue-specific patterns in epithelial tissues, *Am. J. Physiol. 279*, G613−621.
11. Rundle, C. H., and Kappen, C. (1999) Developmental expression of the murine Prl-1 protein tyrosine phosphatase gene, *J. Exp. Zool. 283*, 612−617.
12. Matter, W. F., Estridge, T., Zhang, C., Belagaje, R., Stancato, L., Dixon, J., Johnson, B., Bloem, L., Pickard, T., Donaghue, M., Acton, S., Jeyaseelan, R., Kadambi, V., and Vlahos, C. J. (2001) Role of PRL-3, a human muscle-specific tyrosine phosphatase, in angiotensin-II signaling, *Biochem. Biophys. Res. Commun*. *283*, 1061−1068.
13. Zeng, Q., Dong, J. M., Guo, K., Li, J., Tan, H. X., Koh, V., Pallen, C. J., Manser, E., and Hong, W. (2003) PRL-3 and PRL-1 promote cell migration, invasion, and metastasis, *Cancer Res. 63*, 2716−2722.
14. Werner, S. R., Lee, P. A., DeCamp, M. W., Crowell, D. N., Randall, S. K., and Crowell, P. L. (2003) Enhanced cell cycle progression and down regulation of p21(Cip1/Waf1) by PRL tyrosine phosphatases, *Cancer Lett. 202*, 201−211.
15. Wang, Q., Holmes, D. I., Powell, S. M., Lu, Q. L., and Waxman, J. (2002) Analysis of stromal-epithelial interactions in prostate cancer identifies PTPCAAX2 as a potential oncogene, *Cancer Lett*. *175*, 63−69.
16. Saha, S., Bardelli, A., Buckhaults, P., Velculescu, V. E., Rago, C., St. Croix, B., Romans, K. E., Choti, M. A., Lengauer, C., Kinzler, K. W., and Vogelstein, B. (2001) A phosphatase associated with metastasis of colorectal cancer, *Science 294*, 1343−1346.
17. Kato, H., Semba, S., Miskad, U. A., Seo, Y., Kasuga, M., and Yokozaki, H. (2004) High expression of PRL-3 promotes cancer cell motility and liver metastasis in human colorectal cancer: a predictive molecular marker of metachronous liver and lung metastases, *Clin. Cancer Res. 10*, 7318−7328.
18. Miskad, U. A., Semba, S., Kato, H., and Yokozaki, H. (2004) Expression of PRL-3 phosphatase in human gastric carcinomas: close correlation with invasion and metastasis, *Pathobiology 71*, 176−184.
19. Wu, X., Zeng, H., Zhang, X., Zhao, Y., Sha, H., Ge, X., Zhang, M., Gao, X., and Xu, Q. (2004) Phosphatase of regenerating liver-3 promotes motility and metastasis of mouse melanoma cells, *Am. J. Pathol*. *164*, 2039−2054.
20. Guo, K., Li, J., Tang, J. P., Koh, V., Gan, B. Q., and Zeng, Q. (2004) Catalytic domain of PRL-3 plays an essential role in tumor metastasis: formation of PRL-3 tumors inside the blood vessels, *Cancer Biol. Ther*. *3*, 945−951.
21. Kozlov, G., Cheng, J., Ziomek, E., Banville, D., Gehring, K., and Ekiel, I. (2004) Structural insights into molecular function of the metastasis-associated phosphatase PRL-3, *J. Biol. Chem. 279*, 11882−11889.
22. Jeong, D. G., Kim, S. J., Kim, J. H., Son, J. H., Park, M. R., Lim, S. M., Yoon, T. S., and Ryu, S. E. (2005) Trimeric structure of PRL-1 phosphatase reveals an active enzyme conformation and regulation mechanisms, *J. Mol. Biol. 345*, 401−413.
23. Zhang, Z.-Y., and Van Etten, R. L. (1991) Pre-steady-state and steady-state kinetic analysis of the low molecular weight phosphotyrosyl protein phosphatase from bovine heart, *J. Biol. Chem. 266*, 1516−1525.
24. Otwinowski, Z., and Minor, W. (1997) Processing of X-ray diffraction data collected in oscillation mode, *Methods Enzymol*. *276*, 307−326.
25. Terwilliger, T. C. (1994) MAD phasing: Bayesian estimates of F(A), *Acta Crystallogr., Sect. D: Biol. Crystallogr*. *50*, 11−16.
26. Terwilliger, T. C. (1994) MAD phasing: treatment of dispersive differences as isomorphous replacement information, *Acta Crystallogr., Sect. D: Biol. Crystallogr*. *50*, 17−23.
27. Terwilliger, T. C., and Berendzen, J. (1996) Correlated phasing of multiple isomorphous replacement data, *Acta Crystallogr., Sect. D: Biol. Crystallogr*. *52*, 749−757.
28. Jones, T. A., and Kjeldgaard, M. (1993) *O*, version 5.9, Uppsala University, Uppsala.
29. Brünger, A. T., Adams, P. D., Clore, G. M., DeLano, W. L., Gros, P., Grosse-Kunstleve, R. W., Jiang, J. S., Kuszewski, J., Nilges, M., Pannu, N. S., Read, R. J., Rice, L. M., Simonson, T., and Warren, G. L. (1998) Crystallography & NMR system: A new software suite for macromolecular structure determination, *Acta Crystallogr., Sect. D: Biol. Crystallogr*. *54*, 905−921
30. Wang, W.-Q., Bembenek, J., Gee, K. R., Yu, H., Charbonneau, H., and Zhang, Z.-Y. (2004) Kinetic and Mechanistic Studies of a Cell Cycle Protein Phosphatase Cdc14, *J. Biol. Chem*. *279*, 30459−30468.
31. Holm, L., and Sander, C (1993) Protein structure comparison by alignment of distance matrices. *J. Mol. Biol. 233*, 123−138.
32. Gray, C. H., Good, V. M., Tonks, N. K., and Barford, D. (2003) The structure of the cell cycle protein Cdc14 reveals a proline-directed protein phosphatase, *EMBO J. 22*, 3524−3535.
33. Song, H., Hanlon, N., Brown, N. R., Noble, M. E., Johnson, L. N., and Barford, D. (2001) Phosphoprotein-protein interactions revealed by the crystal structure of kinase-associated phosphatase in complex with phosphoCDK2, *Mol. Cell 7*, 615−626.
34. Lee, J. O., Yang, H., Georgescu, M. M., Di Cristofano, A., Maehama, T., Shi, Y., Dixon, J. E., Pandolfi, P., and Pavletich, N. P. (1999) Crystal structure of the PTEN tumor suppressor: implications for its phosphoinositide phosphatase activity and membrane association, *Cell 99*, 323−334.
35. Yuvaniyama, J., Denu, J. M., Dixon, J. E., and Saper, M. A. (1996) Crystal structure of the dual specificity protein phosphatase VHR, *Science 272*, 1328−1331.
36. Kim, K. A., Song, J. S., Jee, J., Sheen, M. R., Lee, C., Lee, T. G., Ro, S., Cho, J. M., Lee, W., Yamazaki, T., Jeon, Y. H., and Cheong, C. (2004) Structure of human PRL-3, the phosphatase associated with cancer metastasis, *FEBS Lett*. *565*, 181−187.
37. Hancock, J. F., Paterson, H., Marshall, C. J. (1990) A polybasic domain or palmitoylation is required in addition to the CAAX motif to localize p21ras to the plasma membrane, *Cell 63*, 133−139.
38. Murray, D., Ben-Tal, N., Honig, B., and McLaughlin, S. (1997) Electrostatic interaction of myristoylated proteins with membranes: simple physics, complicated biology, *Structure 5*, 985−989.
39. Choy, E., Chiu, V. K., Silletti, J., Feoktistov, M., Morimoto, T., Michaelson, D., Ivanov, I. E., and Philips, M. R. (1999) Endomembrane trafficking of ras: the CAAX motif targets proteins to the ER and Golgi, *Cell 98*, 69−80.
40. Zhang, Z.-Y. (1995) Kinetic and mechanistic characterization of a mammalian protein tyrosine phosphatase, PTP1, *J. Biol. Chem. 270*, 11199−11204.
41. Zhang, Z.-Y., Malachowski, W. P., Van Etten, R. L., and Dixon, J. E. (1994) The nature of the rate-determining steps of the *Yersinia* protein tyrosine phosphatase-catalyzed reactions, *J. Biol. Chem. 269*, 8140−8145.
42. Zhang, Z.-Y., Wu, L., and Chen, L. (1995) Transition state and rate-limiting step of the reaction catalyzed by the human dual specificity phosphatase, VHR, *Biochemistry 34*, 16088−16096.
43. Zhang, Z.-Y. (2003) Mechanistic studies on protein tyrosine phosphatases, *Prog. Nucleic Acid Res. Mol. Biol. 73*, 171−220.
44. McCain, D. F., Catrina, I. E., Hengge, A. C., and Zhang, Z.-Y. (2002) The catalytic mechanism of Cdc25A phosphatase, *J. Biol. Chem. 277*, 11190−11200.
45. Chen, L., Montserat, J., Lawrence, D. S., and Zhang, Z.-Y. (1996) VHR and PTP1 protein phosphatases exhibit remarkably different active site specificities toward low molecular weight nonpeptidic substrates, *Biochemistry 35*, 9349−9354.
46. Gottlin, E. B., Xu, X., Epstein, D. M., Burke, S. P., Eckstein, J. W., Ballow, D. P., and Dixon, J. E. (1996) Kinetic analysis of the catalytic domain of human cdc25B, *J. Biol. Chem. 271*, 27445−27449
47. Zhou, B., and Zhang, Z.-Y. (1999) Mechanism of mitogen-activated protein kinase phosphatase-3 activation by ERK2, *J. Biol. Chem. 274*, 35526−35534.
48. Fjeld, C. C., Rice, A. E., Kim, Y., Gee, K. R., and Denu, J. M. (2000) Mechanistic basis for catalytic activation of mitogen-

activated protein kinase phosphatase 3 by extracellular signal-regulated kinase, *J. Biol. Chem. 275*, 6749−6757.
49. Rudolph, J., Epstein, D. M., Parker, L., and Eckstein, J. (2001) Specificity of natural and artificial substrates for human Cdc25A, *Anal. Biochem. 289*, 43−51.
50. Zhang, Z. Y., Wang, Y., Wu, L., Fauman, E. B., Stuckey, J. A., Schubert, H. L., Saper, M. A., and Dixon, J. E. (1994) The Cys-$(X)_5$Arg catalytic motif in phosphoester hydrolysis, *Biochemistry 33*, 15266−15270.
51. Guo, X.-L., Shen, K., Wang, F., Lawrence, D. S., and Zhang, Z.-Y. (2002) Probing the molecular basis for potent and selective protein tyrosine phosphatase 1B inhibition, *J. Biol. Chem. 277*, 41014−41022.
52. Stewart, A. E., Dowd, S., Keyse, S. M., and McDonald, N. Q. (1999) Crystal structure of the MAPK phosphatase Pyst1 catalytic domain and implications for regulated activation, *Nat. Struct. Biol. 6*, 174−181.
53. Denu, J. M., and Tanner, K. G. (1998) Specific and reversible inactivation of protein tyrosine phosphatases by hydrogen peroxide: evidence for a sulfenic acid intermediate and implications for redox regulation, *Biochemistry 37*, 5633−5642.
54. van Montfort, R. L., Congreve, M., Tisi, D., Carr, R., and Jhoti, H. (2003) Oxidation state of the active-site cysteine in protein tyrosine phosphatase 1B, *Nature 423*, 773−737.
55. Salmeen, A., Andersen, J. N., Myers, M. P., Meng, T. C., Hinks, J. A., Tonks, N. K., and Barford, D. (2003) Redox regulation of protein tyrosine phosphatase 1B involves a sulphenyl-amide intermediate, *Nature 423*, 769−773.
56. Lee, S.-R., Yang, K.-S., Kwon, J., Lee, C., Jeong, W., and Rhee, S. G. (2002) Reversible inactivation of the tumor suppressor PTEN by H_2O_2, *J. Biol. Chem. 277*, 20336−20342.
57. Fauman, E. B., Cogswell, J. P., Lovejoy, B., Rocque, W. J., Holmes, W., Montana, V. G., Piwnica-Worms, H., Rink, M. J., and Saper, M. A. (1998) Crystal structure of the catalytic domain of the human cell cycle control phosphatase, Cdc25A, *Cell 93*, 617−625.
58. Reynolds, R. A., Yem, A. W., Wolfe, C. L., Deibel, M. R., Jr., Chidester. C. G., and Watenpaugh, K. D. (1999) Crystal structure of the catalytic subunit of Cdc25B required for G2/M phase transition of the cell cycle, *J. Mol. Biol. 293*, 559−568.
59. Chiarugi, P., Fiaschi, T., Taddei, M. L., Talini, D., Giannoni, E., Raugei, G., and Ramponi, G. (2001) Two vicinal cysteines confer a peculiar redox regulation to low molecular weight protein tyrosine phosphatase in response to platelet-derived growth factor receptor stimulation, *J. Biol. Chem. 276*, 33478−33487.
60. Kosen, P. A. (1992) in *Stability of Protein Pharmaceuticals* (Ahern, T. J., and Manning, M. C., Eds.) p 34, Plenum Press, New York.
61. Finkel, T. (2003) Oxidant signals and oxidative stress, *Curr. Opin. Cell Biol. 15*, 247−254.
62. Chiarugi, P., and Cirri, P. (2003) Redox regulation of protein tyrosine phosphatases during receptor tyrosine kinase signal transduction, *Trends Biochem. Sci. 28*, 509−514.
63. Nicholls, A., and Honig, B. (1991) A rapid finite difference algorithm, utilizing successive over-relaxation to solve the Poisson-Boltzmann equation, *J. Comput. Chem. 12*, 435−445.

BI0509191